

554841
p 26

NASA Contractor Report 185197

Viscous Three-Dimensional Analyses for Nozzles for Hypersonic Propulsion

G.J. Harloff, D.R. Reddy,
and H.T. Lai

Sverdrup Technology, Inc.
NASA Lewis Research Center Group
Cleveland, Ohio

January 1990

Prepared for
Lewis Research Center
Under Contracts NAS3-24105 and NAS3-25266



National Aeronautics and
Space Administration

(NASA-CR-185197) VISCOUS THREE-DIMENSIONAL
ANALYSES FOR NOZZLES FOR HYPERSONIC
PROPULSION Final Report (Sverdrup
Technology) 25 p

CSCL 21E

N90-17635

63/07 Unclas
0264834

VISCOUS THREE-DIMENSIONAL ANALYSES FOR NOZZLES FOR HYPERSONIC PROPULSION

G.J. Harloff, D.R. Reddy, and H.T. Lai
Sverdrup Technology Inc.
NASA Lewis Research Center Group
Cleveland, Ohio 44135

SUMMARY

E-5267
A Navier-Stokes computer code has been validated using a number of two- and three-dimensional configurations for both laminar and turbulent flows. The validation data covers a range of freestream Mach numbers from 3 to 14, includes wall pressures, velocity profiles, and skin friction. Nozzle flowfields computed for a generic scramjet nozzle from Mach 3 to 20, wall pressures, wall skin friction values, heat transfer values, and overall performance are presented. In addition, three-dimensional solutions obtained for two asymmetric, single expansion ramp nozzles at a pressure ratio of 10 consist of the internal expansion region in the converging/diverging sections and the external supersonic exhaust in a quiescent ambient environment. The fundamental characteristics that have been captured successfully include expansion fans; Mach wave reflections; mixing layers; and nonsymmetrical, multiple inviscid cell, supersonic exhausts. Comparison with experimental data for wall pressure distributions at the center planes shows good agreement.

NOMENCLATURE

a sound speed
 C_f skin friction coefficient
 C_h heat transfer coefficient
 C_p specific heat
 C_v velocity coefficient
M Mach number
NPR Nozzle Pressure Ratio
n nozzle efficiency
 Pr Prandlt number
 P_w local wall static pressure, $P_w/P(0)$
 Re Reynolds number
T temperature
X streamwise distance
 γ ratio of specific heats

Subscripts:

c combustor exit
e nozzle exit
l laminar
n unit normal
o freestream condition
s static condition
t total condition
t turbulent
w wall
 μ viscosity
 ρ density

INTRODUCTION

Accurate evaluation of nozzle performance is essential to hypersonic propulsion because that performance is highly sensitive to net thrust. Highly integrated fuselage/nozzle configurations may experience complex interaction of shocks, turbulent mixing, differing levels of under/over expansion, and possible boundary layer separation. To simulate these complex interactions, the full Navier-Stokes equations need to be solved and the appropriate computer code carefully calibrated before it can be applied to the hypersonic nozzle flow field. The goal of the current study is to validate the PARC3D code over a range of flowfield conditions and to examine the flow physics and overall nozzle performance over a wide range of flight conditions. The PARC3D code solves the full, three-dimensional Reynolds averaged Navier-Stokes equations in strong conservation form with the Beam and Warming approximate factorization algorithm; the implicit scheme uses central differencing for a curvilinear set of coordinates. The code was originally developed as AIR3D by Pulliam and Steger;¹ Pulliam later added Jamison's artificial dissipation and called it ARC3D.² Cooper³ then adapted the ARC3D code for internal propulsion and renamed the code PARC3D.

Code Validation

To gain confidence with the PARC3D code simulating the interaction phenomena characteristic of hypersonic nozzle flow, experimental data were selected for code validation as follows: a two-dimensional shock boundary layer interaction at Mach 14 (Holden⁴), and a Haack-Adams body (Allen⁵) with a favorable pressure gradient at Mach 3. Previous configurations examined at NASA Lewis by Reddy and Harloff⁶ include: a two- and a three-dimensional hypersonic nozzle at $M_0 = 5$, for which comparisons were made with computations of Spradley⁷ and others; and a three-dimensional corner flow configuration at $M_0 = 2.94$ of Oskam et al.⁸ The Reddy and Harloff⁶ study provided confidence in the PARC codes for a variety of complex shapes and high speeds.

Two-Dimensional Shock-Boundary Layer Interaction at Mach 14

The two-dimensional experimental data⁴ at Mach 14 are used as the first test case. The flat plate length was 1.44 ft, the ramp angle was 18° , and the ramp length was 1.14 ft. The Reynolds number per foot, based on total conditions, was 32×10^6 and the computational grid 399×99 . The predicted surface pressure coefficient and skin friction are compared to the test data (Figs. 1 and 2): good agreement for both is evident. The predicted negative skin friction for the separated zone is also in good agreement with experiment. As the boundary layer in the experiment was laminar, this study validates the code at hypersonic conditions for laminar flow.

Haack-Adams Body at Mach 3, Turbulent

The axisymmetric Haack-Adams body,⁵ was 3 ft long, had a length to diameter ratio of 10, and a base to maximum diameter ratio of 0.532. The freestream Mach number was 2.96 and the Reynolds number based on static conditions 0.1×10^6 cm. Detailed velocity measurements were made at 7 axial stations. Comparison of measured and computed velocity profiles at stations 2 and 7 (Figs. 3 and 4) are in excellent agreement with each other. Axial stations shown in Figs. 3 and 4 were at 0.28 and 0.97 of the body length, respectively. The streamwise pressure gradient is favorable for this configuration, which is similar to the nozzle flow environment. The computed C_f (Fig. 5) shows excellent agreement with experimental data. This study validates the Baldwin-Lomax turbulence model used in the PARC3D code for attached axisymmetric flow at a single Mach number.

NOZZLE FLOWFIELD CALCULATIONS

Two-Dimensional Flowfield Calculations, Mach 5, Laminar

A generic three-dimensional nozzle⁷ is shown schematically in Fig. 6. Its length was six entrance nozzle heights, the upper wall has a 20° slope, the lower splitter length was three. The lower wall was horizontal up to one, where the wall expands at a 6° angle. The flow was assumed to be laminar. The grid used was 199×99 .

The nozzle entrance flow was assumed to be uniform, and the ratio of specific heats 1.27 for both streams, the nozzle entrance velocity 1610 m/sec., the static pressure 9206 N/m^2 , the static temperature $2311 \text{ }^\circ\text{K}$, and the Mach number 1.657. The corresponding freestream values were: 1765 m/sec, 506 N/m^2 , $261 \text{ }^\circ\text{K}$, and 5.0, respectively. Upper wall static pressures and values from the GIM code, the Seagull code,⁹ and the Method of Characteristics (MOC)⁹ are shown in Fig. 7. Pressures near the nozzle entrance are in agreement with the GIM results, but are higher in the aft region. The inviscid results of Seagull and MOC lie between the current viscous solution and the GIM solution in this region. The predicted flowfield is presented in terms of Mach number in Fig. 8. The contact surface between the nozzle flow and the freestream deflects downward, as is evident in the total pressure contour plot and the velocity vectors.⁹ Three-dimensional calculations were also performed for this nozzle.⁶

Two-Dimensional Flowfield, Mach 3 to 20, Turbulent

Figure 9 shows the nozzle geometry used in this study. The initial divergence angle is about 37° .

Freestream and Combustor Exit Properties

The ratio of specific heats, γ , and the gas constant of the combustor exit are considered constant throughout the entire flowfield (Table I). Because the static nozzle entrance Reynolds numbers, based on nozzle entrance height, are such that turbulent flow is expected for the entire range of Mach numbers studied, turbulent flow is assumed in the whole flowfield.

GRID

The grid used was 199×129 , uniform in the x -direction (Fig. 10). Grids were clustered by being stretched by hyperbolic functions near the upper and lower walls to resolve the boundary layers, as well as downstream of the cowl to resolve the shear layer. The grid was not adapted to the shear layer location, although this has been accomplished by the authors in previous unpublished studies, which indicated that the present grid was sufficient to capture the flowfield.

Boundary conditions are uniform inflow and extrapolated outflow properties for supersonic flow. The supersonic/hypersonic inflow boundary above the exit was assumed to be uniform. For subsonic outflow, the pressure is imposed by the sublayer approximation. These boundary conditions are ideal and more realistic inflow profiles can be accounted for. The wall temperature is assumed to be constant at 1750°R .

Mach 3 Flowfield

Velocity vectors for $M_0 = 3$ (Fig. 11) show that the flow is overexpanded and a shock propagates from the cowl lip to the upper nozzle wall. The exhaust flows along the upper nozzle wall similar to a wall jet. A slight separation occurs on the upper wall ahead of the shock (discussed below in terms of C_D). The Mach number contours are shown in Fig. 12. Due to the overexpanded flow at the end of the lower cowl, the shear layer turns upward, which causes a shock to form above it.

Total pressure contours shown in Fig. 13 illustrate the gradient in nozzle and freestream total pressure across the shear layer.

The divergence of velocity provides a scalar measure of density gradients such that compressive and expansive regions of the flow can be visualized as dark and light regions respectively (Fig. 14). The deflection angle of the shock from the cowl end to the upper nozzle wall is about 39° and the Mach number in front of the oblique shock is about 3.5. After the shock reflects off the boundary layer, it propagates in the downstream direction. The boundary layer separates on the upper nozzle wall ahead of the incident shock (further illustrated with the skin friction prediction below). Details of this region show a small region of reverse flow. As the shock interacts with the wall boundary layer, it initially reflects at a sharp angle. As the flow moves over the surface of the separation bubble, it is turned less, as shown by the decrease in magnitude of the compression. At the aft end of the separation bubble, the flow is again turned at a sharp angle and coalesces into the reflected shock downstream of the separation. Below the cowl, a shock emanating from the leading edge of the cowl is observed, and is caused by flow deflection from the boundary layer along the lower cowl wall. The expanding region of the flow downstream of the cowl is also observed.

Wall pressures as a function of X for the three nozzle wall surfaces (Fig. 15(a)) illustrate that the wall pressure initially decreases with increasing X for both upper and lower nozzle walls. The interior nozzle shock intersects the upper nozzle wall at about 2.8 ft, as evidenced by the marked pressure rise there. Because the pressure beneath the cowl is greater than the pressure in the nozzle, the shock forms in the nozzle.

Wall skin friction values are shown in Fig. 15(b) for the three surfaces. The skin friction on the upper nozzle wall becomes negative at about 2.8 ft, indicating a small region of reverse flow. The skin friction of the upper cowl wall is slightly higher than that of both the upper and lower walls. The heat transfer for the upper and lower nozzle walls is similar over the cowl's length (Fig. 15(c)) while the rise in the heat transfer coefficient is observed at $X = 2.8$ ft, where the boundary layer flow separates. In the nozzle the heat transfer is positive, indicating hot gas and a cold wall, but below the cowl the heat transfer coefficient is negative, indicating the reverse.

A large scale separation on the upper nozzle surface is predicted for laminar flow (Fig. 16), whereas the turbulent computations show a small separation.

Mach 6 Flowfield

Figure 17 shows the velocity vectors for $M_0 = 6$. The flow, slightly overexpanded at the cowl exit, expands behind the cowl by means of an expansion fan. The wake is deflected upward, as indicated by the velocity vector angles and the position of the velocity shear layer. No reverse flow at the upper boundary is indicated. Mach number contours for the flowfield (Fig. 18) also indicate the location of the shear layer while Fig. 19 shows its upward deflection as well as total pressure contours.

Wall pressures (Fig. 20(a)) show that the interior wall pressure is overexpanded. The wall skin friction and heat transfer values are shown in Figs. 20(b) and (c) respectively.

Mach 10 Flowfield

The exhaust flow is underexpanded at Mach 10 as indicated by the downward deflection of the nozzle flow (Fig. 21). There are no indications of shocks inside the nozzle, but a shock propagates from the lower cowl lip downward due to the underexpansion of the flow (Fig. 22). The total pressure contours at $M_0 = 10$ (Fig. 23) show that the flow is underexpanded and that the shear layer is deflected downward. The shock deflection angle is about 18° . Pressure is constant on the lower wall (Fig. 24(a)), C_f and C_h wall values are also shown in Fig. 24.

Mach 20 Flowfield

The velocity vectors are deflected downward aft of the cowl due to underexpansion (Fig. 25) which causes a shock to propagate from the lower cowl downward. The lower cowl leading edge shock merges with the trailing edge shock about 26 percent of a cowl length downstream of the cowl.

The flow along the curved upper nozzle surface turns and compresses, like flow along a curved ramp, and a curved shock forms inside the nozzle. An upwardly deflected shock behind the end of the upper nozzle wall is evident (Figs. 25 and 26). The Mach number contours are shown in Fig. 26. Total pressure contours (Fig. 27) show the downward deflection of the shear layer. The shock is detached from the lower side of the cowl due to the boundary layer there. The shock from the leading edge of the cowl merges with the shock from the aft end about 18 percent of the length downstream of the cowl. An interior shock along the upper wall turns the flow towards the horizontal axis. This interior shock is typical at overspeed conditions. The nozzle flow is underexpanded (Fig. 28(a)); the upper wall pressure does not follow the lower nozzle wall pressure but instead increases the full length of the nozzle, even inside the cowl. The C_f and C_p values are shown in Fig. 28(b) and (c) respectively.

A perfect gas model has been assumed in these calculations, and the constant ratio of specific heats (γ) has been varied with flight Mach number. This assumption may not be as valid at high Mach numbers as at low Mach numbers and should be further investigated.

Nozzle Performance

The adiabatic nozzle efficiency, N , is the ratio of the nonisentropic to isentropic expansion enthalpies between the combustor exit, c , and the nozzle exit, e . The velocity coefficient, C_v , is the ratio of the actual to the isentropic velocity and is the square root of the efficiency. The velocity coefficient increases with Mach number up to M_0 of 10 but decreases at M_0 of 20. For example, C_v is 0.93 at M_0 of 3, 0.98 at M_0 of 6, 1.0 at M_0 of 10 and 0.94 at M_0 of 20. The reported C_v values peak at M_0 of 10 because the nozzle design Mach number is close to 10 and the M_0 20 is an overspeed condition for this nozzle. The frozen gas assumption has been successfully used for ramjet, rocket, and hypersonic wind tunnel nozzle flows. Because these values might be different with chemistry accounted for, the above C_v values should be considered as relative. For example, Ref. 11 has reported that finite-rate chemical recombination of dissociated species affects scramjet nozzle force coefficients, at Mach 20, and that the nozzle flow analyzed was in vibrational equilibrium.

Three-Dimensional, Single Expansion Ramp Nozzle, NPR = 10, Laminar

Three-dimensional solutions of a single expansion ramp nozzle are performed to simulate the nonaxisymmetric nozzle flowfield in both internal/external expansion regions and the exhaust plume in a quiescent ambient environment. Two different configurations of the nozzle at NPR = 10 are examined. They were selected from the single expansion ramp nozzles experimentally investigated by Re and Leavitt¹¹ to analyze the effects of various geometrical parameters and pressure ratios on the nozzles' static performance.

The present converging/diverging nozzle has a long upper surface functioning as an external expansion ramp, with a rectangular cross-section in the internal nozzle. The edge of the flat sidewall is highly skewed at the nozzle exit to connect the upper and

lower surface lips. The flow generated by large streamwise pressure differences expands from near reservoir conditions through the nozzle and exhausts supersonically into the quiescent air. The resulting flowfield is characterized by flow expansion inside the nozzle and by exhaust plume interaction with the ambient environment. In particular, a strongly interactive flow structure containing a normal shock, expansion/compression wave reflection, and separation can occur along the external expansion ramp of the upper surface. Around this section, the free shear layer emerging from the lip of the shorter lower surface acts as an artificial nozzle wall, and its trajectory shape can alter the nature of the flow, depending on the ambient conditions below it. The wave structure initiated by the shear layer may include an oblique shock or an expansion fan emanating from the lower nozzle lip. This shear layer can also deflect the flow upwards at a high angle to interact with the upper boundary layer.

A similar pattern exists in the spanwise direction, where the sidewall creates a vertical free shear surface starting at the skewed nozzle exit. At high Reynolds number, the shear layer behind a sharp or blunt trailing edge may not be stable; however high Reynolds number interaction of the free shear layer is even more unstable in a quiescent external environment than in a subsonic or supersonic external stream. Consequently, a steady state solution may not be possible for certain flows with a quiescent external stream. The three-dimensionality of the flowfield, its unsteadiness, and stability considerations are some of the complications of the present problem, although only steady-state solutions are computed.

Converged solutions are compared with the experimental measurements for the pressure distributions on the upper and lower nozzle surfaces. The configuration of the nozzle (Fig. 29) has an upper two-dimensional flap and a shorter, lower two-dimensional flap, both flat in the spanwise direction. Part of the upper flap extending from the throat area functions as an external expansion ramp. The edge of the vertical sidewall is highly inclined. This arrangement gives a rectangular cross section parallel to the exit plane aligned with the tilted edge. Intersections of the tilted edge and the upper and lower nozzle walls normally occur upstream of the ends of the wall surfaces.

Two nozzle configurations are examined (Fig. 30) with identical lower flaps and sidewalls and a nozzle aspect ratio of width to height of 4, with the height measured at the throat. Note that the flow expands to a lower pressure in case 2 because the external expansion ramp is longer. The flat sidewall is assumed to have a very thin thickness (0.0058 cm).

All boundary conditions are treated explicitly. Since a plane of symmetry exists in the spanwise z -direction, only half of the nozzle flowfield is computed. Symmetry conditions are specified on this centerplane. No-slip velocity and an adiabatic wall temperature are imposed on the nozzle surfaces. In the farfield, still air conditions at 101.3 kPa and 300 °K, are fixed at the upper and lower boundaries in the vertical y -direction sufficiently far away from the nozzle; similar boundary conditions are imposed at the farfield in the spanwise direction. In the streamwise x -direction, a stagnation pressure of 1013 kPa and a stagnation temperature of 300 °K are specified at the nozzle entrance. Other variables at this location are computed using the isentropic relationships and a characteristic-like condition extrapolated from the interior. At the outflow boundary, streamwise flux gradients are assumed to be negligible.

For normalization, stagnation quantities at the nozzle entrance are taken as the reference variables. The nozzle throat height and the speed of sound are the reference length and velocity, respectively. The Reynolds number is computed based on these values. The reference temperature, pressure and length are taken to be 300 °K, 1013 kPa, and 2.54 cm, respectively. The corresponding Reynolds number is 5.618 million.

Grid

The simulated flow includes the nozzle interior and exterior, which contains the downstream exhaust. Since the nozzle has a symmetrical plane at the middle in the spanwise direction, the spanwise regions include the interior half of the nozzle and the flow exterior to the sidewall. The complete domain is then divided correspondingly into subsections to simplify grid generation using an algebraic technique. To resolve the viscous layers, hyperbolic tangent functions are used to cluster grid points in regions near the walls. Patching these separate segments produces a final sheared grid in Cartesian coordinates.

Figure 31(a) illustrates a view of the nonuniform grid in the x -, y -plane along the streamwise direction. The grid clusters near the wall surfaces to the exhaust region behind the inclined nozzle exit. Figure 31(b) presents a detailed view of the same grid showing a high degree of grid nonorthogonality, particularly next to the exit. The skewed grid lines result since one of the vertical curvilinear coordinates aligns with the sidewall tilted edge to simplify the application of the boundary conditions. Spanwise views of the grid distribution in the y - z plane are shown at two different axial locations inside the nozzle (Fig. 32(a)) and downstream in the exhaust plume, (Fig. 32(b)). The vertical coordinates cluster about the interior and exterior surfaces of the sidewall, and are not on a plane with constant x -coordinate.

The flow starts from the nozzle entrance, $X = 0$, where the total pressure is prescribed, expands through the converging/diverging and external ramp sections, and

exhausts into the downstream low/pressure region, which is bounded by quiescent boundaries far from the nozzle. The farfield computational boundaries are approximated at distances of 25, 10, and 8 characteristic lengths in the x-, y- and z-directions, respectively. The solutions discussed below have been computed on a 135 by 120 by 50 grid for both cases. Of these, 60 by 40 by 30 grid points are employed in the nozzle interior. The smallest grid is on the order of 0.001 near the wall regions for the y- and z-directions. This grid gives typically two to four subsonic points in the dominant supersonic viscous layers. For the x-direction, the grid is slightly refined near the nozzle exit and is on the order of 0.01. In the figures discussed below, i and l indicate the streamwise and spanwise grid indices respectively, while x and z represent the corresponding nondimensional coordinates.

Case 1:

The converged result of the first case is presented with Mach number, density, and pressure contours at several streamwise and spanwise cross sections; contours are in equally spaced increments over the entire range of values unless otherwise noted. Mach number contours on the center plane (Fig. 33(a)) show a typical exhaust plume containing a steady-state, multiple inviscid cell pattern in the supersonic exhaust core. The flow is sonic at the throat and highly supersonic at the exit. The first inviscid cell appears very irregular and is bounded by an expansion/compression wave system. Because of the inclined trajectory of the exhaust plume, the Mach waves emanate from the ends of the flap surfaces, where the upper and lower free shear layers, which depart from the nozzle walls at different angles, become the expansion and compression ramps. The lower shear layer is very diffusive and largely due to lack of grid resolution along this shear layer. The first cell has an average Mach number of 2.7, while the Mach numbers near the cell centers of the next two cells are about 2.3 and 2.0, respectively, showing a gradual decay of the core center velocities. The core cells reduce in size and numbers towards the sidewall, (Figs. 33(b) to (d)) whose effects become pronounced (Fig. 33(d)) with the appearance of the initial vertical shear layer. The flow inside the nozzle has very thin viscous layers next to the walls, particularly on the lower surface, and thus appears predominantly inviscid.

The spanwise contour views are shown in Figs. 34(a) to (d). Figure 34(a) presents Mach contours at an axial station in the nozzle area, where the clustered regions indicate the upper, lower, and sidewall surfaces. The contours in Fig. 34(b) are located on the external expansion ramp. The structure includes the lower shear, thin vertical shear, and upper boundary layers. In the exhaust region, these free shear layers become thicker with downstream distance (Figs. 34(c) to (d)) in which the plume boundaries are evident. The density contours at the center plane and on the plane next to the sidewall (Figs. 35(a) to (b)) show a pattern very much like Mach contours but out of phase. Density variation is also small across both shear layers.

This same variation occurs for the pressure (Fig. 36) which decays quickly to the ambient value. The contours (Figs. 35(a) and 36) show a weak wave system in the exhaust core, particularly after the first inviscid cell. Figures 37(a) and (b), and 38 depict typical density and pressure contours in the spanwise direction, plotted with smaller increments for clarity. Note that large variations in density and pressure occur inside the nozzle, and the exhaust flow does not deviate much from the perfectly expanded condition. Finally, comparison made with the measured data (Figs. 39(a) to (b)) for the upper and lower surfaces in the center plane show good agreement for wall pressure distributions.

Case 2:

Solution of the second case is also presented in terms of the contours of the flow variables. Figures 40(a) to (d) depict the basic flow pattern of the supersonic exhaust into quiescent air. For this geometry, the upper plume boundary is well-defined by the very thin free shear layer which follows the upper nozzle contour, and remains nearly at this height downstream. The other shear layer is also deflected downwards and is diffusive. Although the flow expands to about the same maximum Mach number indicated in case 1, the supersonic inviscid core (Fig. 41(a)) is more extensive. As a result, the fluctuating decrease of the core center velocities becomes smaller. Moreover, the flow is highly asymmetric along the exhaust center line. The sidewall (Fig. 41(d)) causes the initial development of the vertical shear layer, which curves irregularly towards the center plane as it progresses downstream since the spanwise velocity component is large and positive in the initial region of the vertical shear layer, but becomes small and negative downstream. The flow behind the inclined exit consists of two small, separate supersonic regions next to the exit plane.

Spanwise views of Mach contours at various axial locations are given in Figs. 41(a) to (d). The interior cross-sectional view (Fig. 41(a)) shows a thicker expansion layer in the lower half of the nozzle. Figures (41(b) to (d)) depict the contours at the axial plane on the external ramp region and the planes in the exhaust region. Density and pressure contours in the streamwise planes are shown in Figs. 42(a) to (b), and 43. A clear indication of the compression/expansion wave reflection can be observed at the first cell boundary Figs. 42(a) and 43 after which the wave structure then becomes very weak with downstream distance. Spanwise variations of density and pressure are illustrated in Figs. 44(a) to (b) and 45. Comparison between the numerical prediction and experiment (Figs. 46(a) to (b)) show very good agreement for the wall pressure distributions in the center plane.

SUMMARY OF RESULTS

The PARC3D computer code has been validated using a number of two- and three-dimensional configurations with both laminar and turbulent flows. The validation data used included wall pressures, velocity profiles, and skin friction. The validation data cover Mach 3 to 14 with shock-boundary layer interaction and/or boundary layer separation.

Two-dimensional nozzle flowfields were computed and overall performance for a representative scramjet nozzle from Mach 3 to 20. Matching the external pressure at the cowl exit is necessary to avoid waves in the nozzle. At M_0 of 3 and 6 the nozzle flow is overexpanded and shocks are inside the nozzle, while the shear layer is deflected upward. The laminar $M_0 = 3$ nozzle flowfield showed a massive separation on the upper ramp surface, whereas the turbulent solutions showed only a small separation. At M_0 of 10 and 20 the nozzle flow is underexpanded and shocks are outside the nozzle, while the shear layer is deflected downward. At $M_0 = 20$, a shock forms inside the nozzle along the upper wall to deflect the flow from the radial to the horizontal direction.

Three-dimensional solutions were obtained for two asymmetric, single expansion ramp nozzles at a pressure ratio of 10. The computed flow consists of the internal expansion region in the converging/diverging sections and the external supersonic exhaust in a quiescent ambient environment. The fundamental characteristics of the flowfields for the prescribed flow conditions were predicted successfully and include expansion fans; Mach wave reflections; mixing layers; and nonsymmetrical, multiple inviscid cell, supersonic exhausts. Comparison with experimental data for wall pressure distributions at the center planes shows good agreement.

ACKNOWLEDGEMENTS

This work was supported by the NASA Lewis Research Center under contracts NAS3-24105 and NAS3-25266.

REFERENCES

1. Pulliam, T.H.; and Steger, J.L.: Implicit Finite-Difference Simulations of Three-Dimensional Compressible Flow. AIAA J., vol. 18, no. 2, Feb. 1980, pp. 159-167.
2. Pulliam, T.H.: Euler and Thin Layer Navier-Stokes Codes: ARC2D, ARC3D. Notes for Computational Fluid Dynamics User's Workshop, The University of Tennessee Space Institute, Tullahoma, TN, UTSI Pub. E02-4005-023-84, 1984, pp. 15.1-15.85.
3. Cooper, G.K.: The Parc Codes: Theory and Usage. AEDC-TR-87-24, Arnold Engineering Development Center, Arnold Air Force Base, TN, Oct. 1987.
4. Holden, M.S.; and Moselle, J.R.: Theoretical and Experimental Studies of the Shock Wave-Boundary Layer Interaction on Compression Surfaces in Hypersonic Flow. CAL Report No. AF-2410-A-1, Calspan Corp., Buffalo, NY, Oct. 1969.
5. Allen, J.M.: Experimental Preston Tube and Law-of-the-Wall Study of Turbulent Skin Friction on Axisymmetric Bodies at Supersonic Speeds. NASA TN D-5660, 1970.
6. Reddy, D.R., and Harloff, G.J.: Three-Dimensional Viscous Flow Computations of High Area Ratio Nozzles for Hypersonic Propulsion. AIAA Paper 88-0474, Jan. 1988.
7. Spradley, L.W.; Anderson, P.G.; and Pearson, M.L.: Computation of Three-Dimensional Nozzle-Exhaust Flow Fields with the GIM Code. NASA CR-3042, 1978.
8. Oskam, B.; Vas, I.E.; and Bogdonoff, S.M.: Oblique Shock Wave/Turbulent Boundary Layer Interactions in Three Dimensions at Mach 3, Part I. AFFDL-TR-76-48-PT-1, June 1976 (Avail NTIS, AD-A033386).
9. Salas, M.D.; and Hunt, J.L. (NASA Langley Research Center): Private Communications regarding the Langley SEAGULL Code, with L.W. Spradley of Lockheed-Huntsville, June 1977.
10. Rizkalla, O.; Chinitz, W.; and Erdos, J.: Calculated Chemical and Vibrational Non-equilibrium Effects in NASP-type Nozzles. AIAA Paper 88-3263, July 1988.
11. Re, R.J.; and Leavitt, L.D.: Static Internal Performance of Single-Expansion-Ramp Nozzles with Various Combinations of Internal Geometric Parameters. NASA TM-86270, 1984.

TABLE I. - FREESTREAM AND COMBUSTOR EXIT PROPERTIES

M_0	T_0, R	$P_0, psia$	M_c	T_c, R	$P_c, psia$	γ	$R, \frac{ft-lb_f}{lb_m \cdot ^\circ R}$
3	390	1.7	1.0	4075	11.9	1.25	62.7
6	393	.4	1.5	4220	10.4	1.19	63.4
10	409	.15	1.9	5403	75.0	1.16	66.0
20	468	.03	4.6	5119	25.9	1.18	88.0

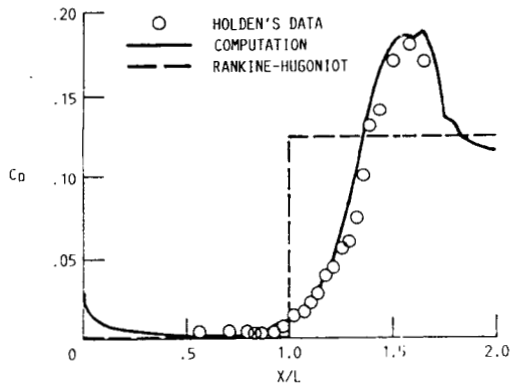


FIGURE 1. - C_D ON 18 DEGREE RAMP AT $M = 14.1$.

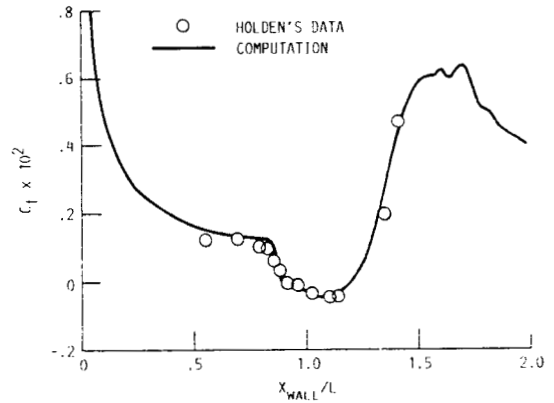


FIGURE 2. - C_L ON 18 DEGREE RAMP AT $M = 14.1$.

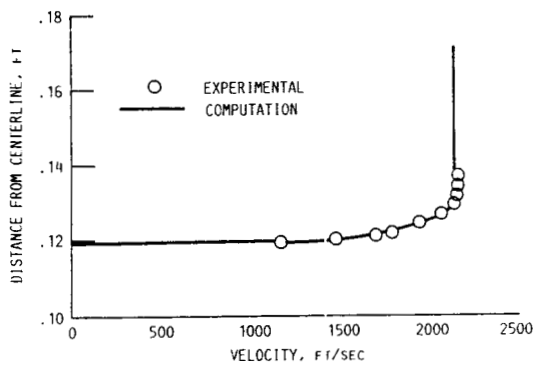


FIGURE 3. - HAACK - ADAMS BODY AT MACH 2.96.
(STATION 2, $X/L = 0.28$).

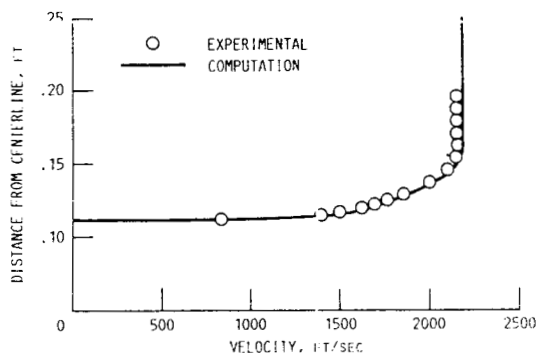


FIGURE 4. - HAACK - ADAMS BODY AT MACH 2.96.
(STATION 7, $X/L = 0.97$).

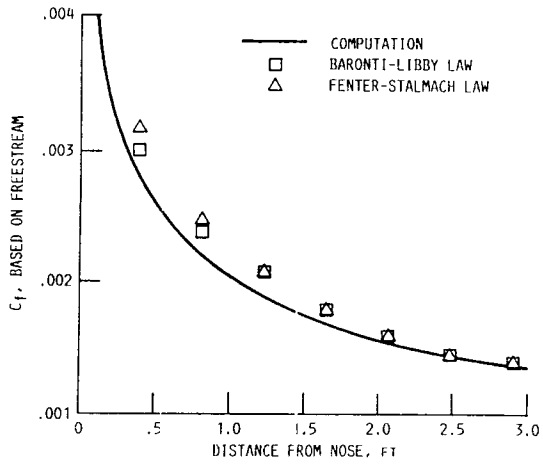


FIGURE 5. - HAACK - ADAMS BODY AT MACH = 2.96.

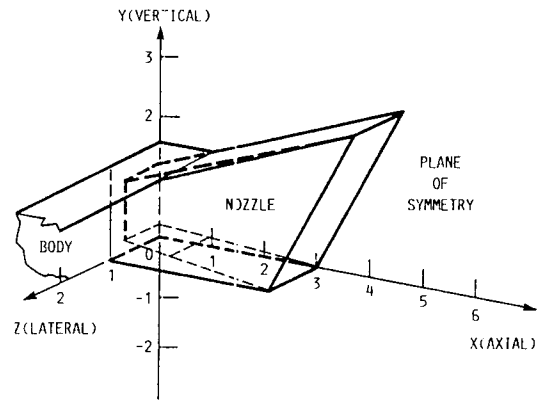


FIGURE 6. - SCHEMATIC OF 3-D NOZZLE.

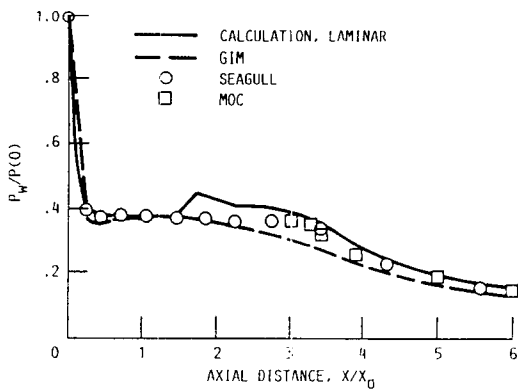


FIGURE 7. - UPPER WALL PRESSURE VERSUS DISTANCE 2-D NOZZLE CALCULATIONS.

- A 0.00
- B 0.50
- C 1.00
- D 1.50
- E 2.00
- F 2.50
- G 3.00
- H 3.50
- I 4.00
- J 4.50

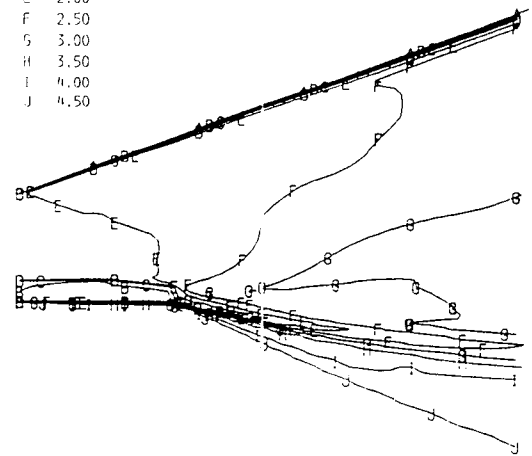


FIGURE 8. - MACH NUMBERS FOR 2-D NOZZLE.

$$Y = A1 + A2 X + A3 X^2 + A4 X^3$$

A1 = .02304
 A2 = .75459
 A3 = -.12370
 A4 = .00600

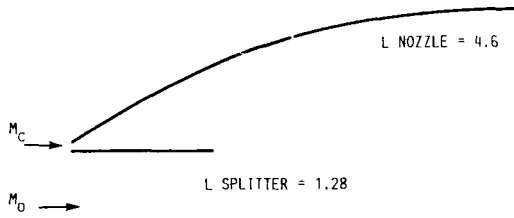


FIGURE 9. - NOZZLE DEFINITION.

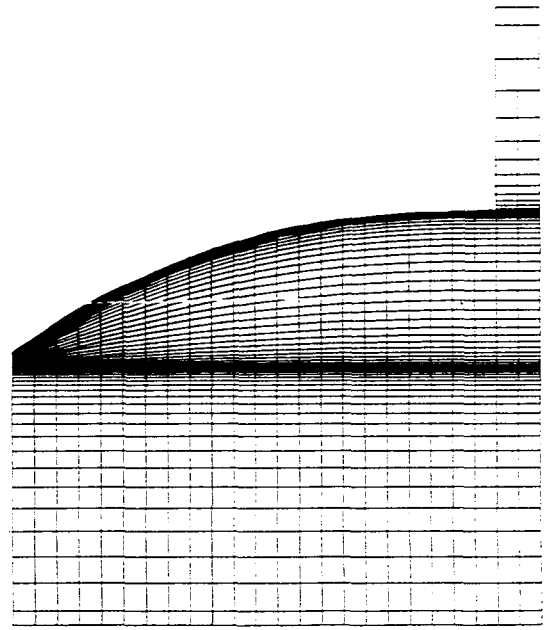


FIGURE 10. - TYPICAL GRID FOR COMPUTATION.

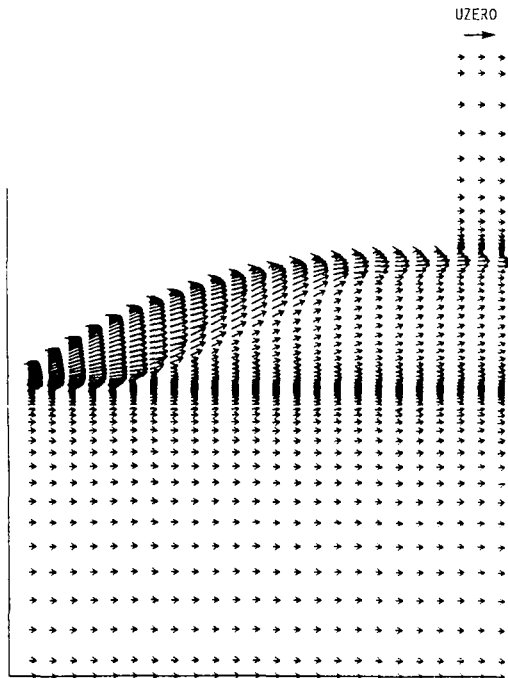


FIGURE 11. - MACH 3, VELOCITY VECTORS.

- A 0.00
- B 0.43
- C 0.86
- D 1.29
- E 1.72
- F 2.16
- G 2.59
- H 3.02
- I 3.45
- J 3.88

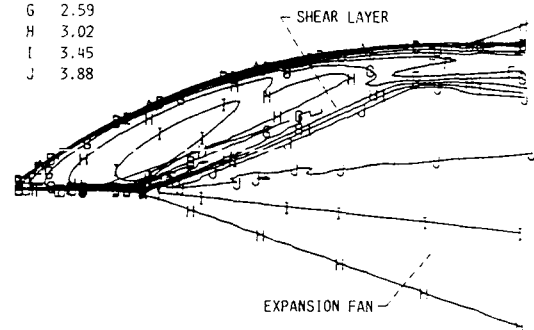


FIGURE 12. - MACH 3, MACH NUMBER CONTOURS.

A	0.00	F	1.75
B	0.35	G	2.11
C	0.70	H	2.46
D	1.05	I	2.81
E	1.40	J	3.16

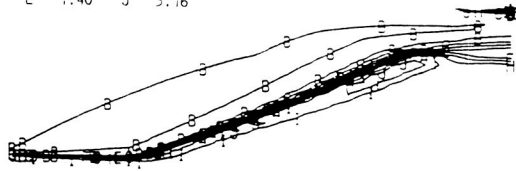


FIGURE 13. - MACH 3, TOTAL PRESSURE CONTOURS.

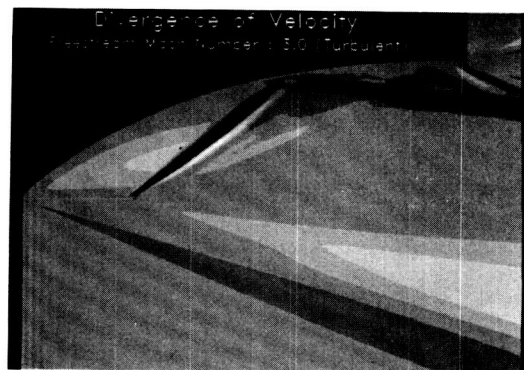


FIGURE 14. - MACH 3, DIVERGENCE OF VELOCITY.

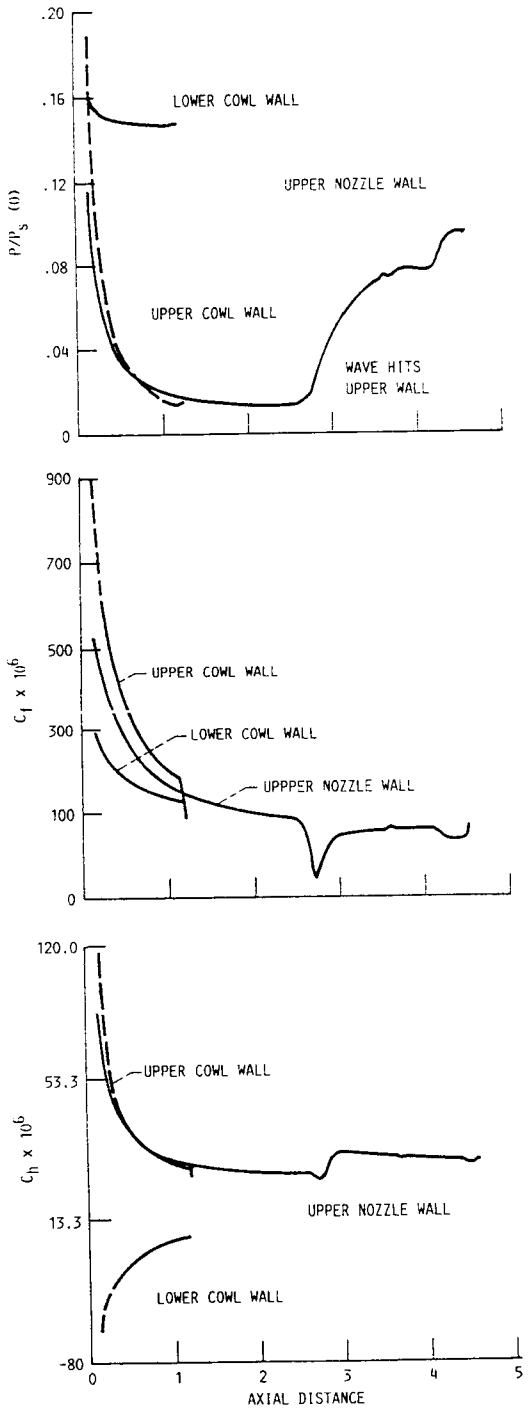


FIGURE 15. - MACH 3. P_w , C_f , C_h VERSUS X.

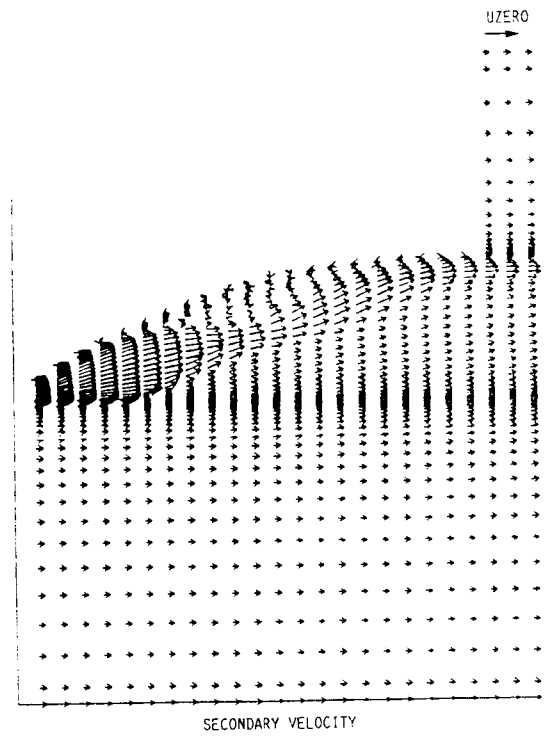


FIGURE 16. - $M_0 = 3$, LAMINAR.

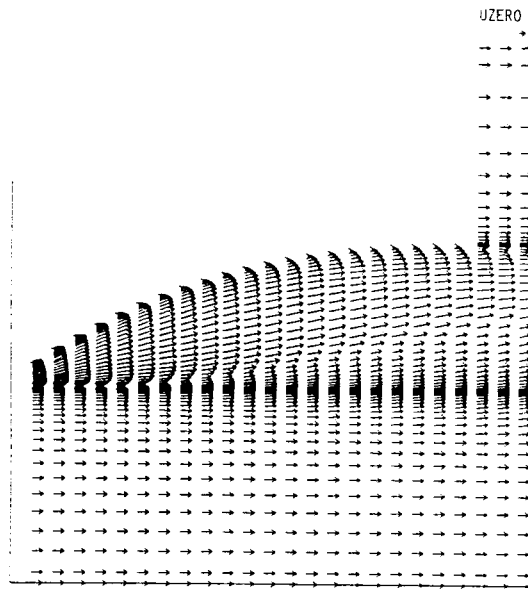


FIGURE 17. - MACH 6. VELOCITY VECTORS.

- A 0.00
- B 0.71
- C 1.42
- D 2.13
- E 2.84
- F 3.55
- G 4.26
- H 4.97
- I 5.68
- J 6.40

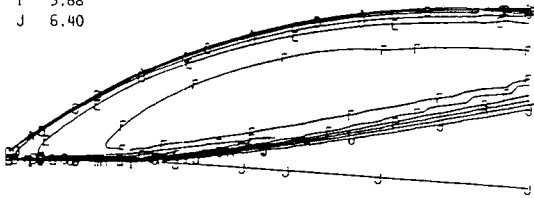


FIGURE 18. - MACH 6, MACH NUMBER CONTOURS.

- A 0.00
- B 15.05
- C 30.11
- D 45.16
- E 60.21
- F 75.26
- G 90.32
- H 105.37
- I 120.42
- J 135.48



FIGURE 19. - MACH 6, TOTAL PRESSURE CONTOURS.

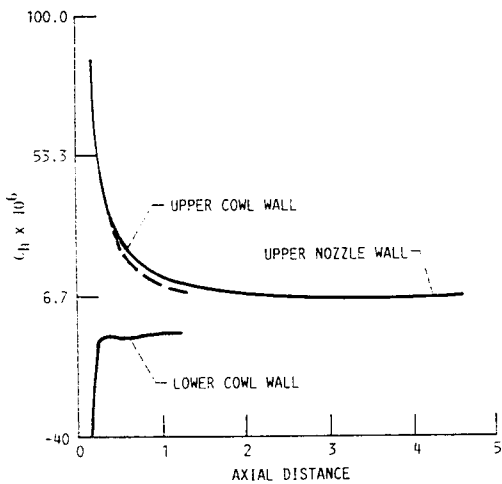
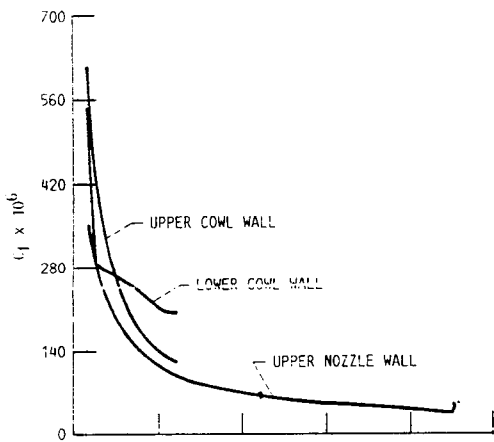
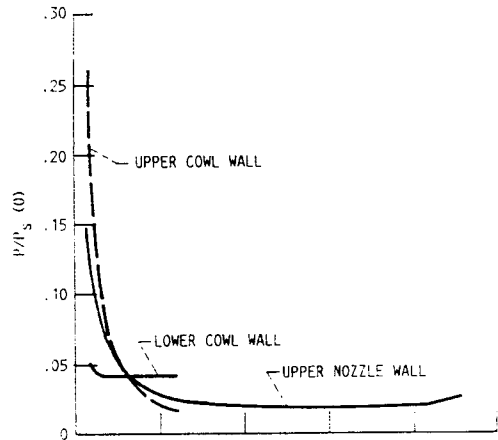


FIGURE 20. - MACH 6. P_w , C_f , C_H VERSUS X.

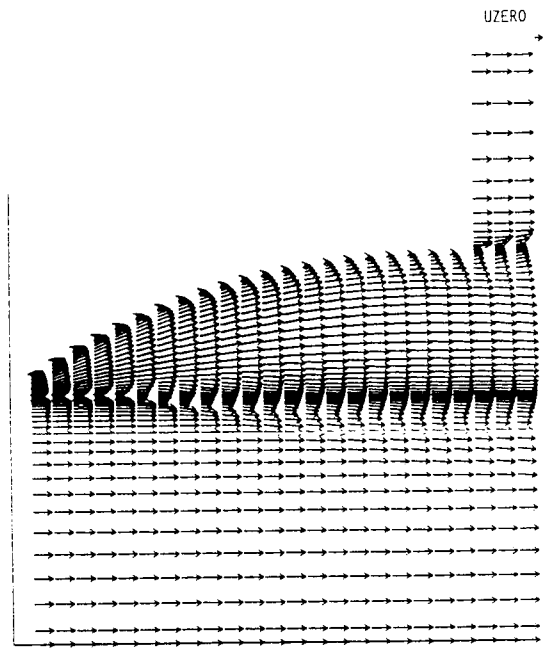


FIGURE 21. - MACH 10, VELOCITY VECTORS.

- A 0.00
- B 1.01
- C 2.03
- D 3.05
- E 4.07
- F 5.08
- G 6.10
- H 7.12
- I 8.14
- J 9.15

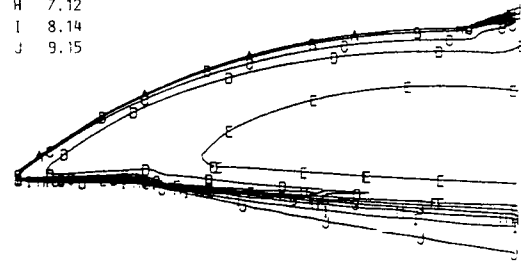


FIGURE 22. - MACH 10, MACH NUMBER CONTOURS.

- A 0.00
- B 240.42
- C 480.85
- D 721.28
- E 961.71
- F 1202.13
- G 1442.56
- H 1682.99
- I 1923.42
- J 2163.84

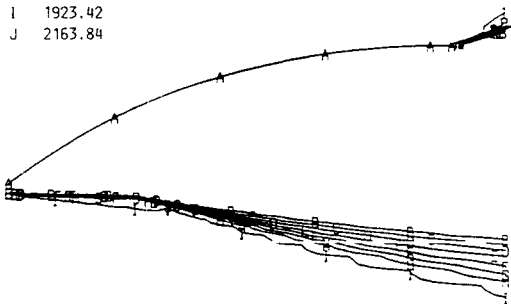


FIGURE 23. - MACH 10, TOTAL PRESSURE CONTOURS.

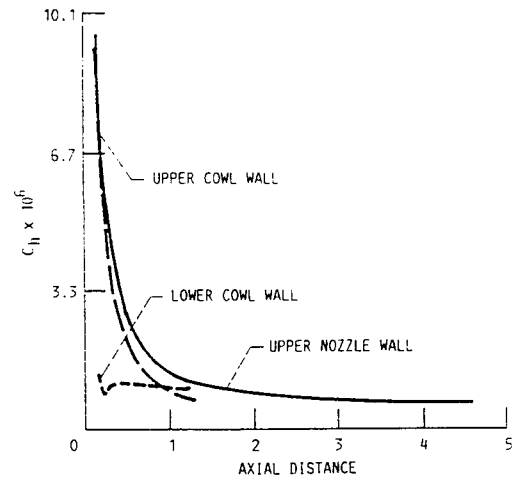
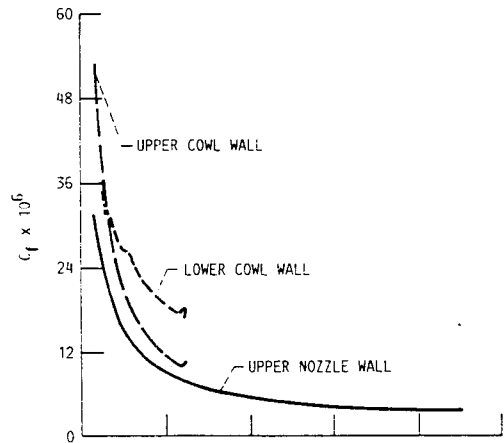
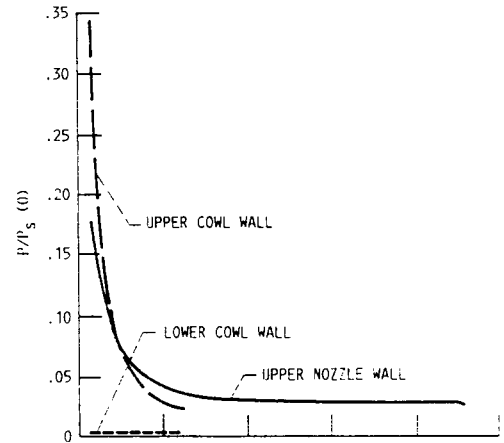


FIGURE 24. - MACH 10, P/P_0 , C_f , C_{H1} VERSUS X.

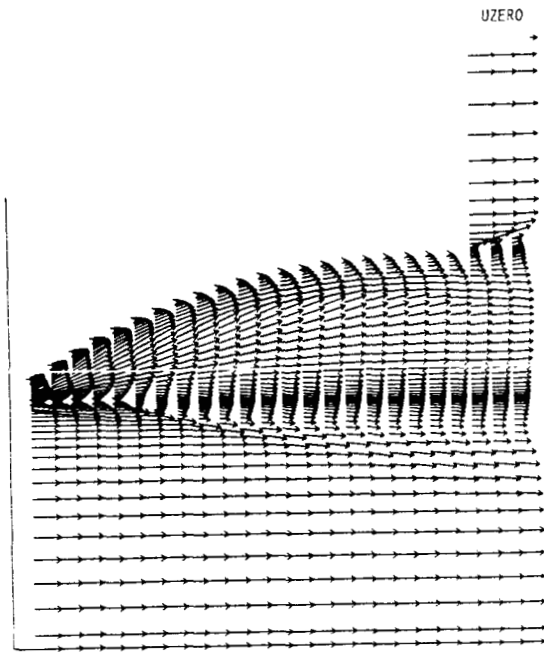


FIGURE 25. - MACH 20, VELOCITY VECTORS.

- A 0.00
- B 2.00
- C 4.00
- D 6.01
- F 8.01
- F 10.02
- G 12.02
- H 14.03
- I 16.03
- J 18.04

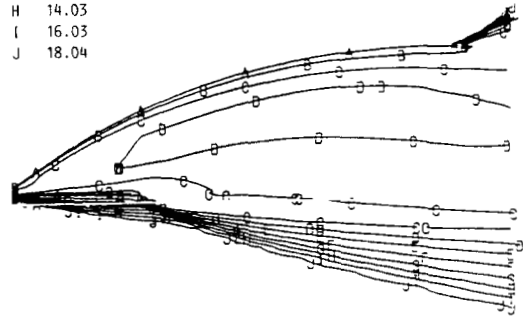


FIGURE 26. - MACH 20, MACH NUMBER CONTOURS.

- A 0.00
- B 1783.24
- C 3566.49
- D 5349.74
- E 7132.99
- F 8916.25
- G 10699.49
- H 12482.74
- I 14265.99
- J 16049.24

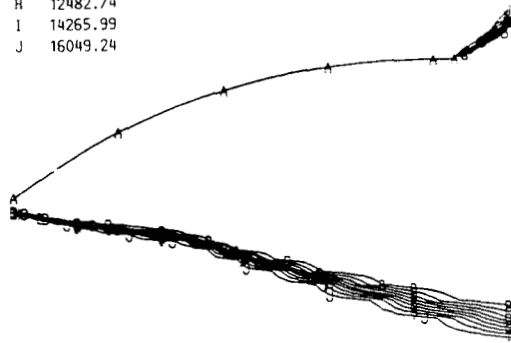


FIGURE 27. - MACH 20, TOTAL PRESSURE CONTOURS.

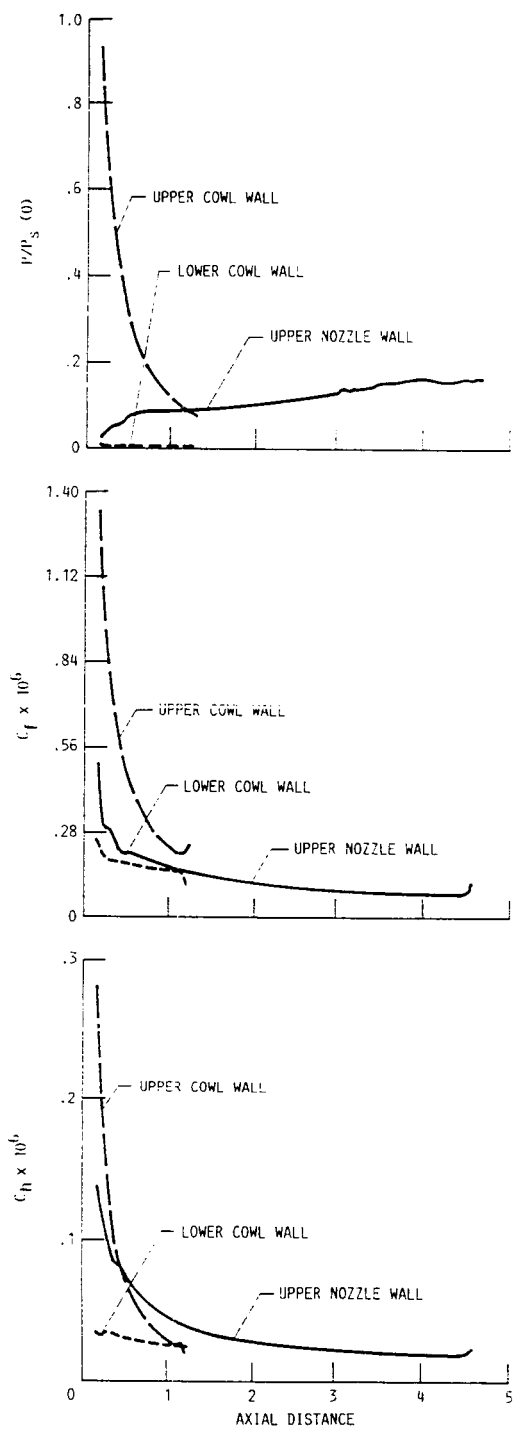


FIGURE 28. - MACH 20. P_w , C_f , C_h VERSUS X.

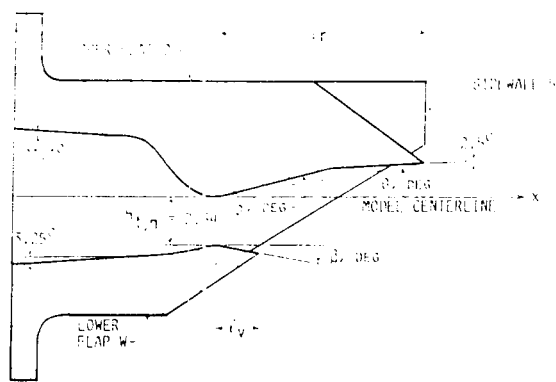


FIGURE 29. - NOZZLE GEOMETRY (FROM REF. 1111).

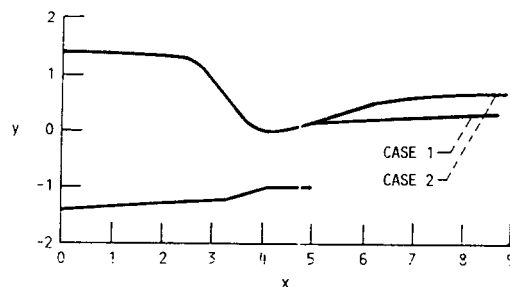
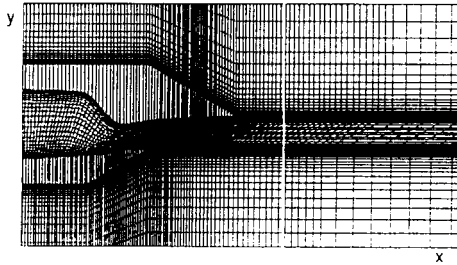
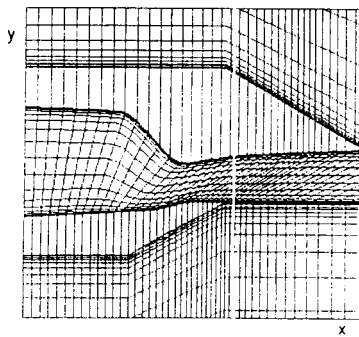


FIGURE 30. - COMPARISON OF TWO NOZZLE CONFIGURATIONS.

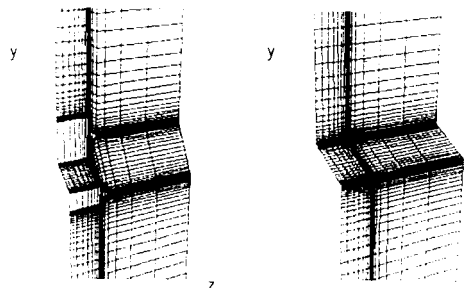


(a) NOZZLE AND EXHAUST GRID.



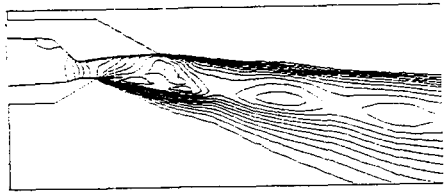
(b) NOZZLE GRID.

FIGURE 31. - STREAMWISE GRID DISTRIBUTIONS.

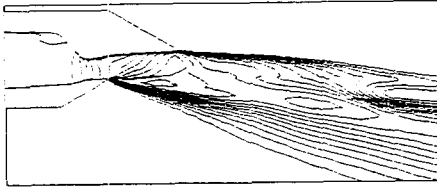


(a) IN THE NOZZLE REGION. (b) IN THE EXHAUST REGION.

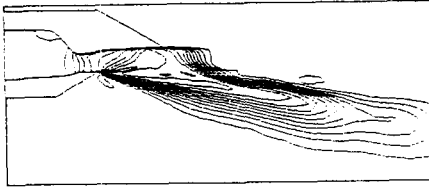
FIGURE 32. - SPANWISE GRID DISTRIBUTION.



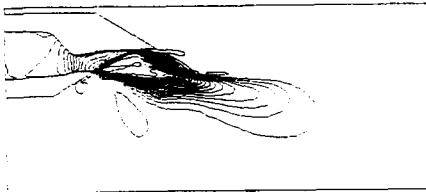
(a) $l = 1, z = 0.$



(b) $l = 9, z = 1.365.$

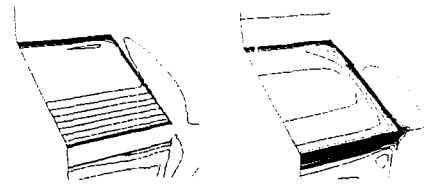


(c) $l = 13, z = 1.7.$



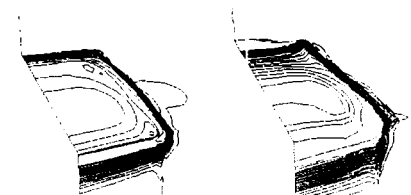
(d) $l = 25, z = 1.982.$

FIGURE 33. - STREAMWISE MACH NUMBER CONTOURS, CASE 1.



(a) $i = 50, x = 4.485.$

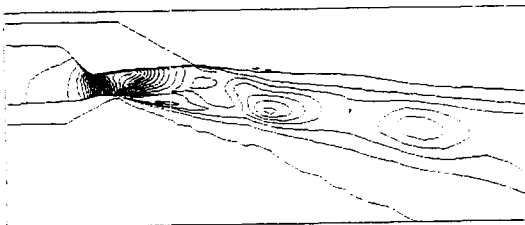
(b) $i = 65, x = 5.372.$



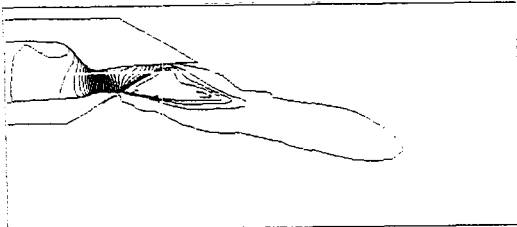
(c) $i = 75, x = 6.221.$

(d) $i = 85, x = 7.513.$

FIGURE 34. - SPANWISE MACH NUMBER CONTOURS, CASE 1



(a) $l = 1, z = 0.0.$



(b) $l = 29, z = 1.998.$

FIGURE 35. - STREAMWISE DENSITY CONTOURS, CASE 1.

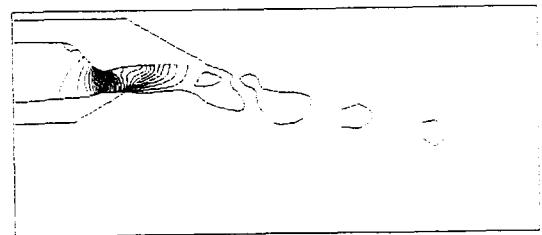
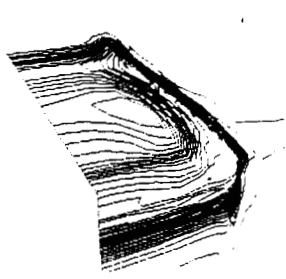
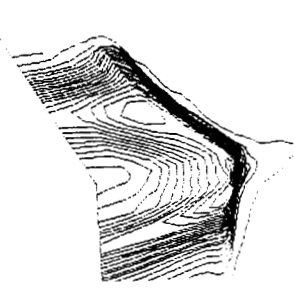


FIGURE 36. - STREAMWISE PRESSURE CONTOURS, CASE 1, $l = 1, x = 0.0.$



(a) $i = 85, x = 7.153$.



(b) $i = 95, x = 9.419$.

FIGURE 37. - SPANWISE DENSITY CONTOURS. CASE 1.

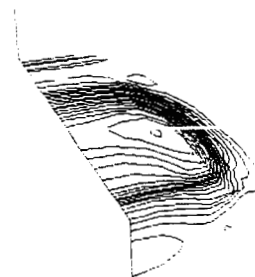


FIGURE 38. - SPANWISE PRESSURE CONTOURS. CASE 1. $i = 85, x = 7.513$.

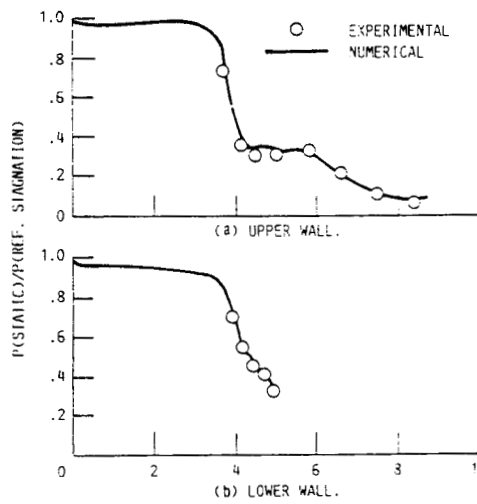


FIGURE 39. - WALL PRESSURE DISTRIBUTIONS. CASE 1.

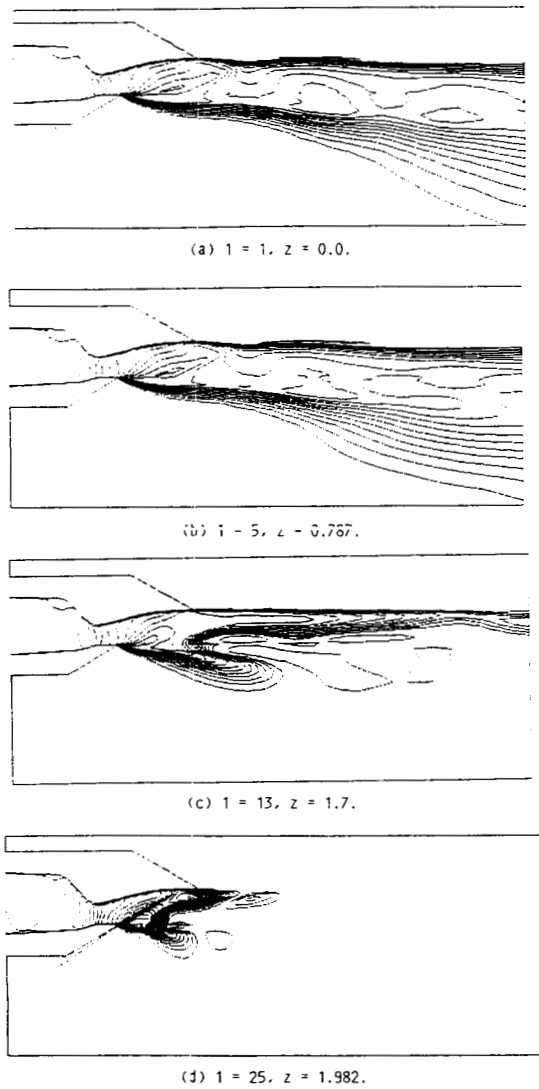


FIGURE 40. - STREAMWISE MACH NUMBER CONTOURS, CASE 2.

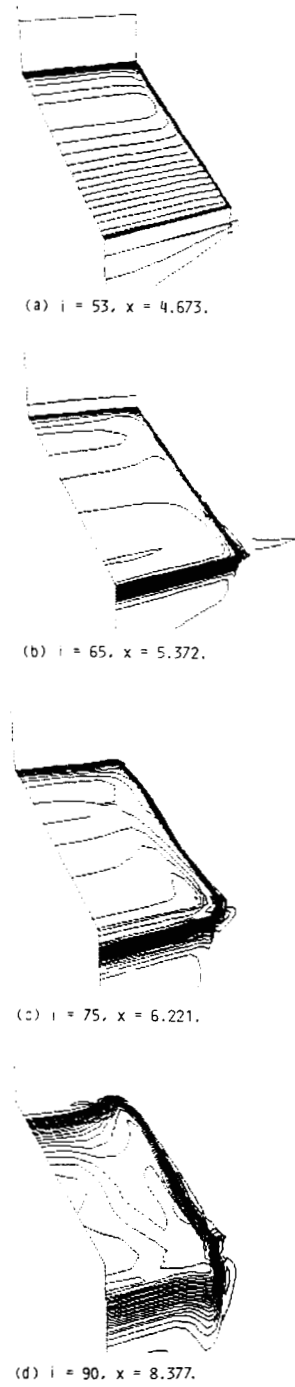
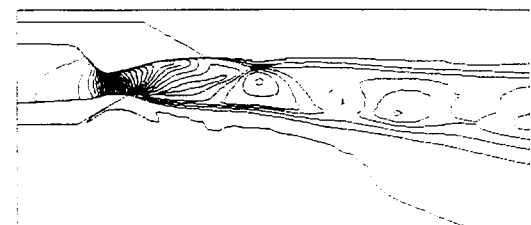
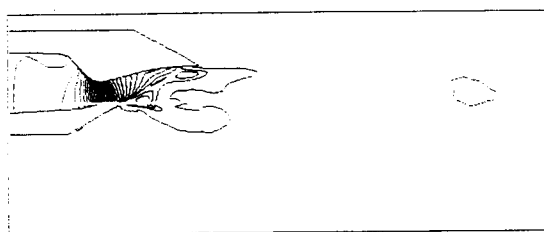


FIGURE 41. - SPANWISE MACH NUMBER CONTOURS, CASE 2.



(a) $t = 1, z = 0.0.$



(b) $t = 29, z = 1.998.$

FIGURE 42. - STREAMWISE DENSITY CONTOURS, CASE 2.

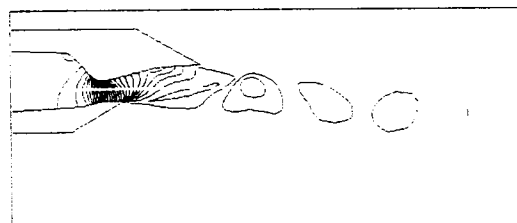
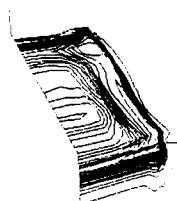
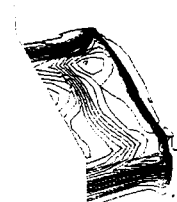


FIGURE 43. - STREAMWISE PRESSURE CONTOURS, CASE 2, $t = 1,$
 $z = 0.0.$



(a) $i = 85, x = 7.513.$



(b) $i = 90, x = 8.377.$

FIGURE 44. - SPANWISE
DENSITY CONTOURS,
CASE 2.

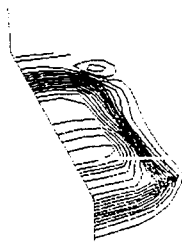


FIGURE 45. - SPANWISE
PRESSURE CONTOURS,
CASE 2. $i = 85$,
 $x = 7.513$.

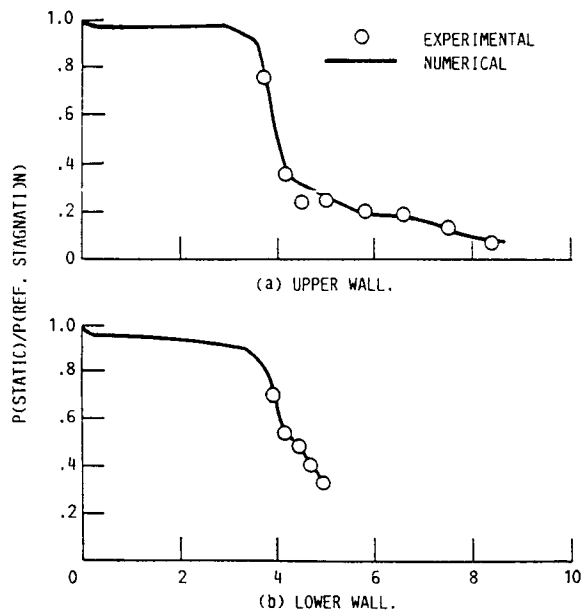


FIGURE 46. - WALL PRESSURE DISTRIBUTIONS, CASE 2.

1. Report No. NASA CR-185197		2. Government Accession No.		3. Recipient's Catalog No.	
4. Title and Subtitle Viscous Three-Dimensional Analyses for Nozzles for Hypersonic Propulsion				5. Report Date January 1990	
				6. Performing Organization Code	
7. Author(s) G.J. Harloff, D.R. Reddy, and H.T. Lai				8. Performing Organization Report No. None (E-5267)	
				10. Work Unit No. 763-01-21	
9. Performing Organization Name and Address Sverdrup Technology, Inc. NASA Lewis Research Center Group Cleveland, Ohio 44135				11. Contract or Grant No. NAS3-24105 and NAS3-25266	
				13. Type of Report and Period Covered Contractor Report Final	
12. Sponsoring Agency Name and Address National Aeronautics and Space Administration Lewis Research Center Cleveland, Ohio 44135-3191				14. Sponsoring Agency Code	
15. Supplementary Notes Project Manager, B.J. Blaha, Propulsion Systems Division, NASA Lewis Research Center. Prepared for the AGARD Symposium on Combined Cycle Propulsion for Hypersonic Application sponsored by the AGARD Propulsion and Energetics Panel, Madrid, Spain, May 21-25, 1990.					
16. Abstract A Navier-Stokes computer code has been validated using a number of two- and three-dimensional configurations for both laminar and turbulent flows. The validation data covers a range of freestream Mach numbers from 3 to 14, includes wall pressures, velocity profiles, and skin friction. Nozzle flowfields computed for a generic scramjet nozzle from Mach 3 to 20, wall pressures, wall skin friction values, heat transfer values, and overall performance are presented. In addition, three-dimensional solutions obtained for two asymmetric, single expansion ramp nozzles at a pressure ratio of 10 consists of the internal expansion region in the converging/diverging sections and the external supersonic exhaust in a quiescent ambient environment. The fundamental characteristics that have been captured successfully include expansion fans; Mach wave reflections; mixing layers; and nonsymmetrical, multiple inviscid cell, supersonic exhausts. Comparison with experimental data for wall pressure distributions at the center planes shows good agreement.					
17. Key Words (Suggested by Author(s)) Hypersonic propulsion Nozzle flow fields			18. Distribution Statement Unclassified—Unlimited Subject Category 07		
19. Security Classif. (of this report) Unclassified		20. Security Classif. (of this page) Unclassified		21. No. of pages 24	22. Price* A03